International Journal of Pharmaceutics: X 10 (2025) 100426

Contents lists available at ScienceDirect

International Journal of Pharmaceutics: X

journal homepage: www.sciencedirect.com/journal/international-journal-of-pharmaceutics-x

Iron-doped Zif-8 nanoplatform for MRI-guided synergistic microwave thermal/chemodynamic therapy of triple-negative breast cancer

Zhenyu Xiang [a,1], Jialing Liu [b,1], Yan Zhang [a], Ru Shen [a], Ying Lu [b,c], Rong Li [b,c], Qinying Shi [b,c], Guannan Zhang [b,c,**], Sijin Li [a,*], Jianbo Song [b,c,**]

[a] Department of Nuclear Medicine, First Hospital of Shanxi Medical University, Shanxi Key Laboratory of Molecular Imaging, Collaborative Innovation Center for Molecular Imaging of Precision Medicine, Shanxi Medical University, Taiyuan 030001, Shanxi Province, PR China
[b] Shanxi Bethune Hospital, Shanxi Academy of Medical Sciences, Third Hospital of Shanxi Medical University, Tongji Shanxi Hospital, Taiyuan 030032, PR China
[c] Shanxi Provincial Key Laboratory for Translational Nuclear Medicine and Precision Protection, Taiyuan 030006, PR China

ARTICLE INFO

Keywords:
Metal-organic framework
Chemodynamic therapy
Microwave thermal therapy
Magnetic resonance imaging
Triple-negative breast cancer

ABSTRACT

Triple-negative breast cancer (TNBC), a highly refractory malignancy characterized by aggressive clinical behavior, poses a significant therapeutic challenge due to its resistance to conventional treatments. While microwave thermal therapy (MWTT) emerges as a promising modality for TNBC treatment through deep-tissue penetration and uniform energy delivery, its reliance on prolonged hyperthermia exposure risks collateral damage to adjacent healthy tissues. Herein, we present a rationally engineered iron-doped zeolitic imidazolate framework-8 nanoplatform (Fe@Zif-8). This study aimed to develop a theranostic agent for MRI-guided combination therapy by pursuing the following objectives: (1) synthesizing and characterizing Fe-doped ZIF-8; (2) evaluating the enhancement of microwave thermal conversion efficiency *via* iron doping; (3) validating the nanoparticle's Fenton catalytic activity for reactive oxygen species (ROS) generation and glutathione depletion in the tumor microenvironment; and (4) demonstrating the synergistic antitumor efficacy of combined MWTT and CDT both *in vitro* and *in vivo*. Accordingly, Fe@Zif-8 was synthesized *via* a one-pot solvothermal method and systematically characterized. Its therapeutic performance was then rigorously assessed through a series of physicochemical and biological experiments. The iron dopants substantially enhance microwave absorption and dielectric loss effects in Zif-8 matrices, enabling Fe@Zif-8 to generate intensified hyperthermia under MW irradiation. Concurrently, iron ions released from the nanoplatform react with endogenous hydrogen peroxide (H_2O_2) *via* Fenton catalysis to produce substantial ROS. The concerted action of MWTT and CDT achieves rapid tumor ablation while significantly reducing therapeutic energy requirements. Furthermore, the platform served as an effective T2 contrast agent for magnetic resonance imaging (MRI), enabling non-invasive monitoring. This work provides a new approach for the preparation of nanomaterials with highly efficient anti-TNBC performance.

1. Introduction

Breast cancer persists as the most common malignancy among women, with triple-negative breast cancer (TNBC) constituting the most aggressive subtype (Schade et al., 2024; Haggag et al., 2022). Epidemiological data from 2022 indicate that TNBC represents approximately 15 % of newly diagnosed invasive breast cancer cases in the United States (Siegel et al., 2022). Conventional TNBC treatments, including chemotherapy, targeted therapy, and immunotherapy, are constrained by substantial limitations such as systemic toxicity, drug resistance, and inadequate therapeutic outcomes, posing significant clinical challenges (Bianchini et al., 2022; Canning et al., 2023; Lancet, 2017; Fu et al., 2019). These shortcomings underscore the imperative to develop innovative therapeutic strategies that transcend traditional modalities.

Recent advancements in tumor ablation techniques driven by exogenous energy sources (*e.g.*, light, ultrasound, microwave) have attracted

* Corresponding author.
** Corresponding authors at: Shanxi Bethune Hospital, Shanxi Academy of Medical Sciences, Third Hospital of Shanxi Medical University, Tongji Shanxi Hospital, Taiyuan 030032, PR China.
E-mail addresses: zhangguannan@sxbqeh.com.cn (G. Zhang), lisjnm123@163.com (S. Li), songjianbo@sxbqeh.com.cn (J. Song).
[1] These authors contributed equally to this work.

https://doi.org/10.1016/j.ijpx.2025.100426
Received 15 July 2025; Received in revised form 17 October 2025; Accepted 22 October 2025
Available online 24 October 2025

considerable attention (Zhu et al., 2023; Truong Hoang et al., 2023; Li et al., 2024). However, combinatorial therapies utilizing light or ultrasound are frequently impeded by tumor microenvironmental hypoxia and uneven heat generation (Kong et al., 2022). In contrast, microwave thermal therapy (MWTT) demonstrates superior advantages in deep tissue penetration, broad therapeutic coverage, and stable thermal output (Li et al., 2022; Li et al., 2023). Metal-organic frameworks (MOFs), constructed from metal ions and organic ligan, have emerged as promising candidates due to their intrinsic characteristics: high specific surface area, tunable porosity, structurally adaptable frameworks, and excellent biocompatibility (Pan et al., 2018; Gong et al., 2022). Moreover, the abundant porous architecture of MOFs facilitates microwave energy dissipation through internal collisions, thereby enhancing MWTT efficiency (Cui et al., 2024). Nevertheless, achieving optimal tumor eradication *via* MWTT alone typically requires prolonged high-temperature exposure, which risks damaging adjacent healthy tissues (Li et al., 2020). Consequently, a critical challenge remains: how to selectively improve MW energy utilization in tumor regions while minimizing off-target thermal injury.

Chemodynamic therapy (CDT), a tumor microenvironment (TME)-activated therapeutic strategy, employs transition metal ions (*e.g.*, Fe, Cu, Mn) to catalyze Fenton or Fenton-like reactions with endogenous hydrogen peroxide (H_2O_2), generating cytotoxic reactive oxygen species (ROS, such as hydroxyl radicals, ·OH) to induce tumor cell death (Cheung and Vousden, 2022; Wang et al., 2020). This approach has demonstrated potential across multiple cancer models, including breast cancer, hepatocellular carcinoma, and glioblastoma (Zhao et al., 2023; Lin et al., 2020; Yuan et al., 2024). The efficacy of CDT can be further amplified by depleting glutathione (GSH), a key antioxidant that scavenges ROS in the tumor microenvironment. Beyond iron-based nanomaterials, various other nanoparticles have been engineered to disrupt the redox balance by simultaneously generating ROS and converting GSH to its oxidized form (GSSG). For instance, manganese- and copper-based nanosystems have demonstrated excellent Fenton-like activity and GSH depletion capabilities, thereby synergistically enhancing oxidative stress-induced apoptosis in cancer cells (Pallavi et al., 2024; Thirumalai et al., 2023; Yang et al., 2024). Among metal catalysts, iron ions exhibit unique merits: (1) broad pH adaptability and high catalytic activity with inherent biocompatibility; (2) strong dielectric and magnetic loss capabilities enabling efficient microwave energy absorption and localized heat generation (Wang et al., 2023; Laha et al., 2022). This thermal effect not only directly ablates tumors but also accelerates iron ion release, reduces TME pH, and stimulates H_2O_2 production, thereby synergistically enhancing Fenton reaction kinetics. Additionally, iron ions induce magnetic field perturbations and alter proton relaxation times, enabling magnetic resonance imaging (MRI) for theranostic integration (Laha et al., 2022).

Hence, we designed an iron ion-doped MOF platform (Fe@Zif-8) for MRI-guided *in situ* TNBC therapy. The iron ion doping strategy achieves dual functions: (1) real-time MRI monitoring of material distribution within tumors and (2) enhanced microwave absorption capacity for combined MWTT and CDT. Under microwave (MW) irradiation, Fe@Zif-8 rapidly eliminates TNBC through microwave-triggered hyperthermia and catalytic ROS generation. As depicted in Scheme 1, we systematically investigated the antitumor performance, mechanism, and theranostic potential of Fe@Zif-8.

2. Materials and methods

2.1. Chemicals and materials

Zinc Nitrate Hexahydrate ($ZnNO_3{\cdot}6H_2O$), 2-Methylimidazole ($C_4H_6N_2$), ferric chloride ($FeCl_3$) and Glutathione (GSH) were obtained from Shanghai Aladdin Biochemical Technology Co., Ltd. (China). Hydrogen peroxide (H_2O_2), 3,3′,5,5’-Tetramethylbenzidine (TMB), 5,5-Dimethyl-1-pyrroline N-oxide (DMPO) and 5,5 Dithiobis (2-

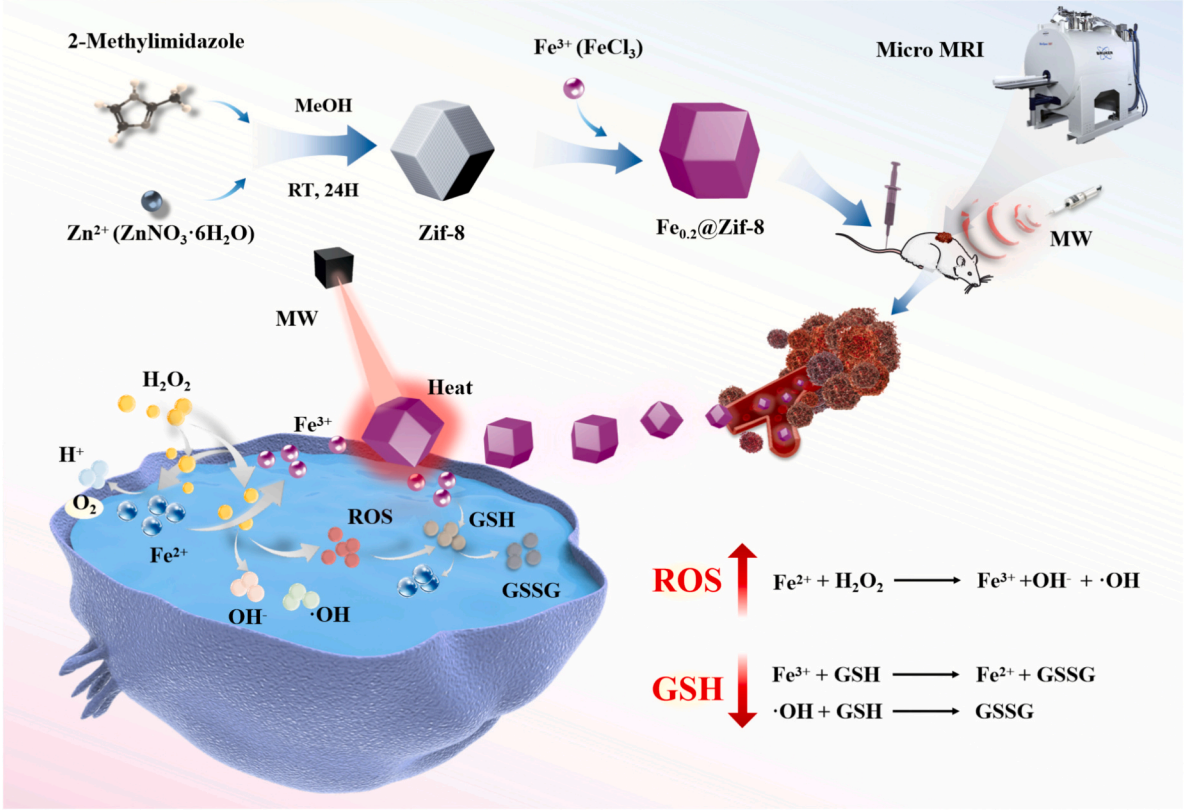

Scheme 1. Schematic illustration of $Fe_{0.2}$@Zif-8 killing TNBC under MW irradiation.

nitrobenzoic acid) (DTNB) was produced by Shanghai Macklin Biochemical Co., Ltd. (China).

2.2. Materials preparation

2.2.1. Preparation of Zif-8

1.5 g of $ZnNO_3{\cdot}6H_2O$ and 2.2 g of $C_4H_6N_2$ were dissolved in 70 mL of methanol and stirred at room temperature for 24 h. The precipitate was then collected by centrifugation, finally washed and dried to obtain Zif-8 crystals.

2.2.2. Preparation of $Fe_{0.1}$@Zif-8, $Fe_{0.2}$@Zif-8 and $Fe_{0.3}$@ Zif-8

In the preparation of Zif-8, 0.1 g,0.2 g and 0.3 g of $FeCl_3$ were added. The products obtained were named $Fe_{0.1}$@Zif-8, $Fe_{0.2}$@Zif-8 and $Fe_{0.3}$@ Zif-8 respectively.

2.3. Materials characterization

The morphology of all materials was determined by field emission scanning electron microscopy (FESEM, JSM-7001F, JEOL) and transmission electron microscopy (Talos, F200, Thermo Scientific). Phase composition was analyzed by X-ray diffraction (XRD, Rigaku Ultima IV, Cu Ka radiation, from 5°to 85°). The surface chemical compositions of Zif-8 and $Fe_{0.2}$@Zif-8 were determined by X-ray photoelectron spectroscopy (XPS, Ka, Thermo).

2.4. Microwave thermal effects of Zif-8 and $Fe_{0.2}$@Zif-8

5 mg of Zif-8 and $Fe_{0.2}$@Zif-8 were placed into 5 mL EP tubes, and 3 mL PBS was added to each EP tube. Each EP tube was irradiated with 5 W of MW for 15 min respectively. Meanwhile, in order to further determine the thermal properties of MW for all the samples, the temperatures of the solutions were recorded using a thermal imaging camera every 5 min. In addition, the temperature of $Fe_{0.2}$@Zif-8 at different masses (1 mg, 2 mg, 5 mg and 10 mg) and different MW powers (1 W, 2 W, 5 W and 10 W) were also measured.

2.5. Electromagnetic measurements of Zif-8 and $Fe_{0.2}$@Zif-8

The dielectric constant and magnetic permeability of Zif-8 and $Fe_{0.2}$@Zif-8 were analyzed using a MW network analyzer and based on the obtained dielectric constant and magnetic permeability the attenuation constant (α), reflection loss (RL), dielectric loss (Tanδε) and magnetic loss (tanδμ) were calculated. The equations are given below:

$$\alpha = \sqrt{2}\ \frac{\pi f}{c}\sqrt{(\mu''\varepsilon'' - \mu'\varepsilon') + \sqrt{(\mu''\varepsilon'' - \mu'\varepsilon')^2 + (\mu'\varepsilon'' - \mu''\varepsilon')^2}} \quad (1)$$

$$\mathrm{RL} = 20\ |\ \frac{Z_{in} - 1}{Z_{in} + 1}\ | \quad (2)$$

$$\tan\delta\varepsilon = \varepsilon'' / \varepsilon' \quad (3)$$

$$\tan\delta\mu = \mu'' / \mu' \quad (4)$$

2.6. The measurement of ROS

The Zif-8 and Zif-8 doped with different levels of Fe were mixed with 100 μL of 1 mg/mL TMB solution, 100 μL of 1 % H_2O_2 and 2 mL of acetate buffer. Meanwhile, the absorbance values of different concentrations of $Fe_{0.2}$@Zif-8 (100, 200 and 500 μg/mL), different irradiation times (5, 10, and 15 min) and different concentrations of H_2O_2 (1 %, 2 %, and 3 %) after the reaction were also measured.

The ROS was also measured by EPR using DMPO as a trapping agent.

2.7. The release of Fe^{3+}

The Zif-8 and $Fe_{0.2}$@Zif-8 were dispersed in ultrapure water at a concentration of 5 mg/mL, and the concentration of Fe^{3+} in the supernatant was measured after 10 min, 20 min, and 30 min of release.

2.8. The degradation of GSH

The different materials were mixed well with 1 mL of 1×10^{-3} M GSH bicarbonate buffer and 100 μL of 0.1 % H_2O_2 solution was added. Then after irradiation with MW for 15 min, 200 μL of 20 μM DTNB and 2 mL of Tris-HCl solution with pH = 8 were added. The absorbance values of the different solutions at 420 nm were measured.

2.9. In vitro toxicity test of $Fe_{0.2}$@Zif-8

The cytotoxicity of the fabricated nanoparticles towards 4 T1 cells was assessed using a Cell Counting Kit-8 (CCK-8) assay. Initially, the cells were seeded into 96-well plates at a density of 5×10^3 cells per well and allowed to grow for 24 h under specified conditions. The culture medium was subsequently substituted with media containing different concentrations of $Fe_{0.2}$@Zif-8. Post incubation, the CCK-8 solution was introduced and the plates were incubated for an additional 2 h. The absorbance at 450 nm was then quantified using a Synergy H1 Microplate Reader. A complete medium served as the control. The biocompatibility of blank Zif-8 nanoparticles was also assessed using the CCK-8 assay for both 4 T1 cells and L929 cells, utilizing protocols parallel to the cytotoxicity evaluations. For the above experiments, each group consisted of three parallel samples and the cell viability was calculated as follows:

$$\text{Cell viability}\,(\%) = (\text{OD test} - \text{OD blank}) / (\text{OD control} - \text{OD blank}) \times 100\%$$

2.10. In vitro antitumor experiment using combined treatments

A standard CCK-8 assay was used to examine the therapeutic effect of $Fe_{0.2}$@Zif-8 in inhibiting tumor cells under combined MWTT and CDT. The cells were divided into control, H_2O_2, $Fe_{0.2}$@Zif-8, and $Fe_{0.2}$@Zif-8 + H_2O_2 groups. The added concentrations of reagents were 100 μg/mL for $Fe_{0.2}$@Zif-8 and 100 μM for H_2O_2. The control group volume was made equal with Dulbecco's modified Eagle's medium (DMEM). After incubation for 24 h, the cells were irradiated under 5 W of microwave for 10 min. Then another incubation was performed for 2 h. Finally, CCK-8 and microplate reader were used by the same process to obtain the cell-viability.

2.11. Live/dead cell staining

Live/dead cell analysis of $Fe_{0.2}$@Zif-8 was performed with cell-permeable dye propidium iodide (PI) and Calcein AM (Beyotime Biotechnology, China) with or without MW irradiation. 4 T1 cells were planted in 6-well plates with a density of 3×10^4 cells per well for 12 h and then were co-incubated with $Fe_{0.2}$@Zif-8 (100 mg/ mL) for 2 h. After gently washing with PBS, the cells were re-cultured with fresh PBS. The microwave ablation probe was then placed vertically under the bottom of each well, and the cells were subjected to microwave irradiation (2450 MHz, 5 W, 10 min or 0 min). Then the 4 T1 cells were stained with PI (red) to visualize dead cells and with Calcein AM (green) to visualize live cells.

2.12. Determination of ROS generation at the cellular level

$Fe_{0.2}$@Zif-8 nanozyme at a concentration of 100 μg/mL was incubated with 4 T1 cells in a 6-well plate for 12 h. Then, the cells were irradiated with MW at 5 W for 10 min. Next, these cells were incubated with DCFH-DA probes at a concentration of 10 μM per well. After 30

min, the excess probes were washed with PBS and the fluorescence was observed by fluorescent microscope. Additionally, the fluorescence intensity was analyzed by flow cytometry, and other experimental operations were completely consistent with the above.

2.13. In vitro cell apoptosis test of $Fe_{0.2}$@Zif-8

Flow cytometry was used to examine the effect of $Fe_{0.2}$@Zif-8 nanospheres on tumor cell apoptosis. The groupings were identical to the live/dead cell staining experiment. The treated cells and the control cells were collected in centrifuge tubes and resuspended in specific buffer solution. To each sample, we simultaneously added fluorescein isothiocyanate (FITC; 5 μL) and propidium iodide (PI) staining solution (5 μL). The reaction was carried out for 15 min. Then, 500 μL of buffer solution was added to the sample tubes. Cell apoptosis was measured using a flow detector.

2.14. Animal studies

The animal experiments were approved by the Animal Ethics Committee of "Shanxi Medical University". Female BALB/c nude mice aged six weeks were utilized in all *in vivo* experiments. Subcutaneous inoculation of 1×10^6 4 T1 cells into the fourth mammary pad was used to establish mouse mammary cancer models. Once the tumors in the tumor - bearing mice reached a volume of 100 mm^3, the mice were included in the subsequent animal experiments. The mice were randomly divided into three groups (Control, Zif-8, $Fe_{0.2}$@Zif-8, $n = 5$ for each group) and injected each with 200 mL of normal saline, Zif-8, or $Fe_{0.2}$@Zif-8 (75 mg/kg), respectively. Then, 6 h post - injection, the Zif-8 and $Fe_{0.2}$@Zif-8 groups were subjected to microwave irradiation (5 W, 10 min). During irradiation, temperature changes were monitored using an IR thermal imager (Hikvision, Hangzhou, China). Tumor volume was measured and mouse weight was recorded every three days. On day 15, the mice were sacrificed, and tumor samples were collected, weighed, and photographed. After being rinsed with PBS, the tumor tissues were fixed in 4 % paraformaldehyde for 24 h. Then, the samples were embedded, sectioned, and stained with H&E, TUNEL, and Ki-67 for immunohistochemical analysis.

2.15. MR imaging

The transverse relaxation (r2) of $Fe_{0.2}$@Zif-8, which quantifies its efficacy as a T2 contrast agent, was determined according to established protocols (Thirumalai et al., 2024). Briefly, aqueous dispersions of $Fe_{0.2}$@Zif-8 with varying Fe concentrations (0.2, 0.4, 0.8, 1.2, and 1.6 mM) were prepared. The T2 relaxation times of these dispersions were measured using a 7.0 T MRI scanner with a multi-spin-echo sequence. The r2 relaxation (in units of mM^{-1} s^{-1}) was calculated as the slope of the linear regression of the relaxation rate ($R2 = 1/T2$) *versus* the Fe concentration.

MRI (7.0 T, Brucker, Germen) was used to observe changes in the image signal and verify whether $Fe_{0.2}$@Zif-8 could function in MRI *in vivo*. $Fe_{0.2}$@Zif-8 solution (30 mg/ kg) was injected into the tail veins of tumor-bearing mice of similar weight and tumor size. We performed MRI sequence T2-FLASH imaging before injection and at 2, 4, 6, 8, and 10 h after injection. By comparing the changes in the signal in the tumor tissues, we evaluated the MRI performance of $Fe_{0.2}$@Zif-8 in this mouse model.

2.16. Statistical analysis

The outcomes were assessed in triplicate and depicted as means ± SD. Statistical analysis was conducted using GraphPad Prism 10 (GraphPad Software, San Diego, CA, USA). In terms of statistical significance, * denotes $p < 0.05$, ** denotes $p < 0.01$, and *** denotes $p < 0.001$.

3. Results and discussion

3.1. Characterization of $Fe_{0.2}$@Zif-8

The morphology of $Fe_{0.2}$@Zif-8 is observed by TEM. As shown in Fig. 1a and b, $Fe_{0.2}$@Zif-8 also exhibits an irregular morphology compared to pristine Zif-8 (Fig. S1), indicating that iron doping does not alter the morphology of the material. From the elemental distribution under HR-TEM(Fig. 1c), Fe, Zn, O and N are uniformly distributed on $Fe_{0.2}$@Zif-8, which indicates that Fe is successfully doped into Zif-8. The FTIR spectra of different samples are shown in Fig. 1d. The absorption peaks of the C═C bond and C═N of the imidazole ring are observed at 1631 cm^{-1} and 1569 cm^{-1} for all samples (Dai et al., 2018). In addition to this, the stretching vibration peaks of C—N bond Zn—N and are found at 1149 cm^{-1} and 1000 cm^{-1} (Li et al., 2019). Therefore, it can be illustrated that the main functional groups of Zif-8 are not destroyed, and the material remains stable after doping with different contents of Fe.

The XRD results of Zif-8 and Zif-8 doped with different levels of Fe are shown in Fig. 1e. The diffraction peaks of Zif-8 at 7.28°, 10.36°, 12.66°, 14.7°, 16.42°, 18.12°, 22.12°, 24.5°, 26.56° and 29.32° correspond to its (011), (002), (112), (022), (013), (222), (114), (233), (134) and (044) crystal planes, respectively (Yang et al., 2021a). This is in agreement with previous reports, indicating that Zif-8 is successfully prepared. The XRD pattern of $Fe_{0.1}$@Zif-8 is basically the same as that of Zif-8, therefore a small amount of Fe doping will not have any effect on Zif-8. However, the XRD pattern of $Fe_{0.2}$@Zif-8 and $Fe_{0.3}$@Zif-8 is changed with the increase of doped Fe content, which indicates that the crystallinity of Zif-8 is altered by the increase of Fe dopin (Wu et al., 2020).

The surface chemical properties of Zif-8 and $Fe_{0.2}$@Zif-8 are analyzed by XPS. The presence of Zn, Fe, N and C elements on the surface of $Fe_{0.2}$@Zif-8 is confirmed in Fig. 1f. Two characteristic peaks belonging to Zn $2p_{3/2}$ and Zn $2p_{1/2}$ can be observed in both Zif-8 and $Fe_{0.2}$@Zif-8 (Fig. S2). As shown in Fig. 1g, the high-resolution Fe 2p XPS spectrum of $Fe_{0.2}$@Zif-8 was deconvoluted to gain insight into the chemical state of iron (Fig. 1g). The spectrum was fitted with characteristic peaks for Fe^{3+} species, following established fitting procedures for iron-containing compounds (Gowtham et al., 2022). The peaks at binding energies of approximately 724.7 eV and 711.2 eV are assigned to Fe $2p_{1/2}$ and Fe $2p_{3/2}$ of Fe^{3+}, respectively. In the C 1 s spectra of Zif-8 and $Fe_{0.2}$@Zif-8, C = C/C-C, C = N, and C—N are both found (Fig. 1h) (Li et al., 2019). Unlike, only pyridine N and pyrrole N can be observed only in the spectrum of N 1 s of Zif-8. In contrast, a Fe—N peak can be observed in the spectrum of N 1 s of $Fe_{0.2}$@Zif-8 in addition to pyridine N and pyrrole (Li et al., 2018), which proves that Fe element is successfully doped into Zif-8 (Fig. 1i).

3.2. MW thermal Response of $Fe_{0.2}$@Zif-8

The energy of MW is mainly converted into heat. As shown in Fig. 2a, the temperature of the control group is increased from 32.6 °C to 61.2 °C under 5 W of MW irradiation. In contrast, the temperatures of Zif-8 and $Fe_{0.2}$@Zif-8 increased to 65.7 °C and 70.2 °C, respectively. This indicates that the thermal effect of $Fe_{0.2}$@Zif-8 is stronger than that of Zif-8 under the same conditions. Meanwhile, the temperature rise curves are measured for different masses of $Fe_{0.2}$@Zif-8 and different MW powers (Fig. S3). Therefore, the $Fe_{0.2}$@Zif-8 has a good thermal effect.

The MW thermal mechanism of $Fe_{0.2}$@Zif-8 can be determined from the reflection loss (RL) values. In general, a smaller RL value means that more MW is absorbed and therefore has a better thermal effec (Jin et al., 2022). At 2.45 GHz, the RL values of Zif-8 and $Fe_{0.2}$@Zif-8 are −2.38 db and − 2.53 db, respectively, indicating that more MW is absorbed by $Fe_{0.2}$@Zif-8 (Fig. 2b and c). In addition, the 3D curves of Zif-8 and $Fe_{0.2}$@Zif-8 also proved that $Fe_{0.2}$@Zif-8 has better MW absorption (Fig. 2d and e). Meanwhile, the α value of $Fe_{0.2}$@Zif-8 (17.45) at 2.45

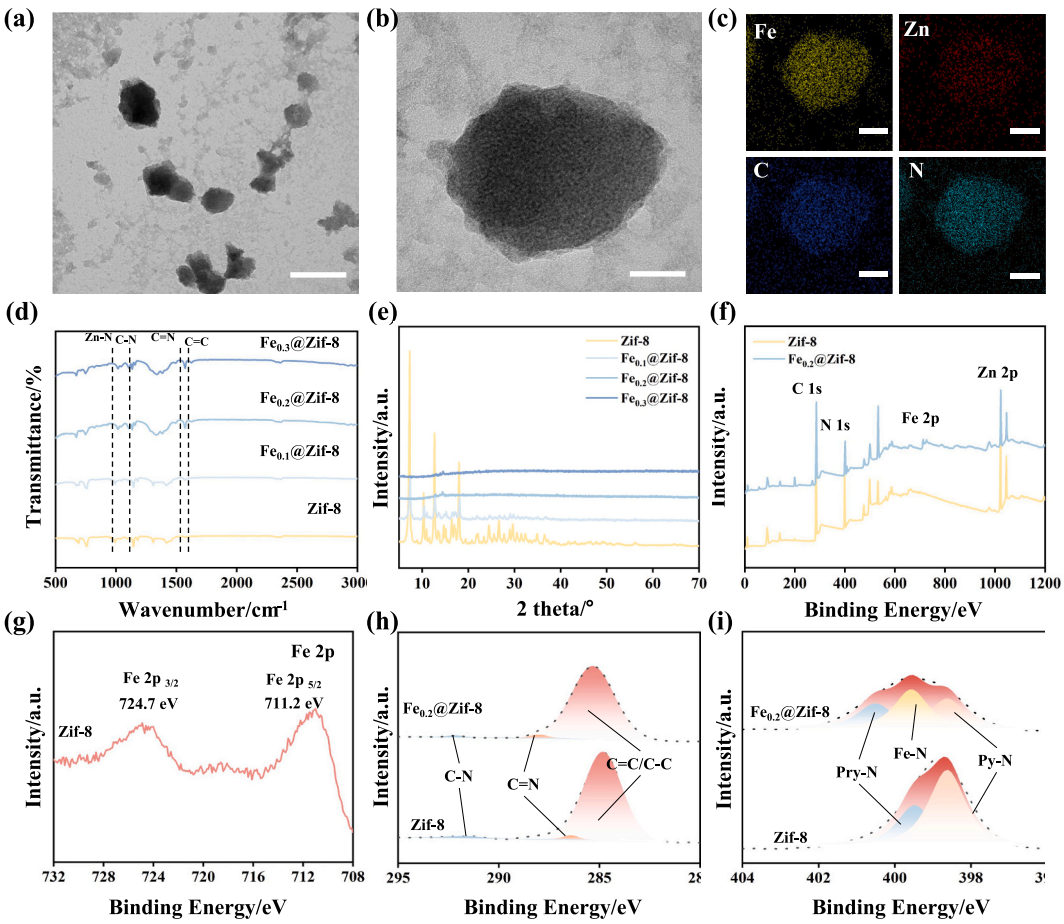

Fig. 1. (a) TEM image (scale bar 200 nm) and (b) HR-TEM image (scale bar 20 nm) of $Fe_{0.2}$@Zif-8; (d) HR-TEM element mapping imagines of $Fe_{0.2}$@Zif-8 (scale bar 20 nm); (d) FTIR spectra and (e) XRD patterns of Zif-8, $Fe_{0.1}$@Zif-8, $Fe_{0.2}$@Zif-8 and $Fe_{0.3}$@Zif-8; (f) XPS spectra of Zif-8 and $Fe_{0.2}$@Zif-8; High-resolution XPS spectra of (g) Fe 3d, (h) C 1 s, and (i) N 1 s.

GHz is larger than that of Zif-8 (16.64). The higher α value proves that more MW is converted into heat (Fig. 2f). Therefore, the $Fe_{0.2}$@Zif-8 has a better thermal effect.

The dielectric constant (ε) and magnetic permeability (μ) of $Fe_{0.2}$@Zif-8 can be used to determine how the MW is converted into heat. As shown in Fig. 2g and h, the values of the real part (ε') of the dielectric constants of $Fe_{0.2}$@Zif-8 is larger than that of Zif-8, while the value of the imaginary part (ε") of Zif-8 and $Fe_{0.2}$@Zif-8 are basically the same. This indicates that the dielectric loss capability of $Fe_{0.2}$@Zif-8 is stronger than Zif-8. Furthermore, the real part value (μ') of magnetic permeability of $Fe_{0.2}$@Zif-8 is slightly larger than that of Zif-8, while the value of the imaginary part (μ") is similar, indicating that the magnetic loss is not the main factor in converting MW into heat (Fig. 2j and k). In addition, the dielectric constant tangent ($\tan\delta\varepsilon = \varepsilon''/\varepsilon'$) and magnetic loss tangent ($\tan\delta\mu = \mu''/\mu'$) can also be utilized to evaluate the incident MW dissipation capabilit (Lv et al., 2023). Among them, the tan δε of $Fe_{0.2}$@Zif-8 is slightly smaller than that of Zif-8. On the contrary, the values of tan δμ of the two samples are close to each other, which indicates that the material has an average magnetic loss capability. In summary, the $Fe_{0.2}$@Zif-8 converts the absorbed MW into heat through dielectric loss.

3.3. ROS Production and GSH Oxidation

Large amounts of H_2O_2 are present in the microenvironment of tumors. H_2O_2 can undergo a Fenton reaction with Fe^{3+} to produce ·OH. 3,3′5,5′-tetramethylbenzidine (TMB) can be used to characterize the results of the Fenton reaction (Jin et al., 2024), since ·OH can oxidize colorless TMB to blue oxidized TMB (Fig. 3a). The catalytic ability of Zif-8 doped with different levels of Fe^{3+} is first tested. As shown in Fig. S4, the absorbance value of the solution at 650 nm is gradually increasing with the increase of Fe^{3+} content and $Fe_{0.2}$@Zif-8 has the largest absorbance value. Therefore, the $Fe_{0.2}$@Zif-8 is selected for the next experiments because $Fe_{0.2}$@Zif-8 has the best Fenton reaction rate.

As shown in Fig. 3b and c, the absorbance value in $Fe_{0.2}$@Zif-8 is much greater than the control and Zif-8 groups, because the release of Fe^{3+} from $Fe_{0.2}$@Zif-8 is capable of Fenton reaction. Meanwhile, the absorbance value in the $Fe_{0.2}$@Zif-8 group is further increased after MW irradiation, indicating that MW can promote the reaction between $Fe_{0.2}$@Zif-8 and H_2O_2. The time of MW irradiation, concentration of $Fe_{0.2}$@Zif-8, and concentration of H_2O_2 can also affect the rate of Fenton reaction. The yield of ·OH is gradually increased with the time of MW irradiation (Fig. 3d and e). As shown in Fig. 3f and g, an increase in the concentration of $Fe_{0.2}$@Zif-8 with or without MW irradiation also enhances the rate of the Fenton reaction. For the same duration of MW irradiation, an increment of H_2O_2 concentration also produces more ·OH (Fig. 3h and i).

Meanwhile, the EPR has also been used to measure the ROS produced by different materials. As shown in Fig. 4a, no signal peaks of ·OH is observed in the control and Zif-8 groups. However, a clear 1:2:1 signal peak of ·OH is observed in the $Fe_{0.2}$@Zif-8 groups. Therefore, $Fe_{0.2}$@Zif-8 produces more ROS.

The release curve of Fe^{3+} from $Fe_{0.2}$@Zif-8 is shown in Fig. 4b. The release of Fe^{3+} from $Fe_{0.2}$@Zif-8 is increasing with time. The GSH inside the tumor protects the tumor cells from being damaged by ROS. The ·OH produced by the Fenton reaction can oxidize GSH to glutathione

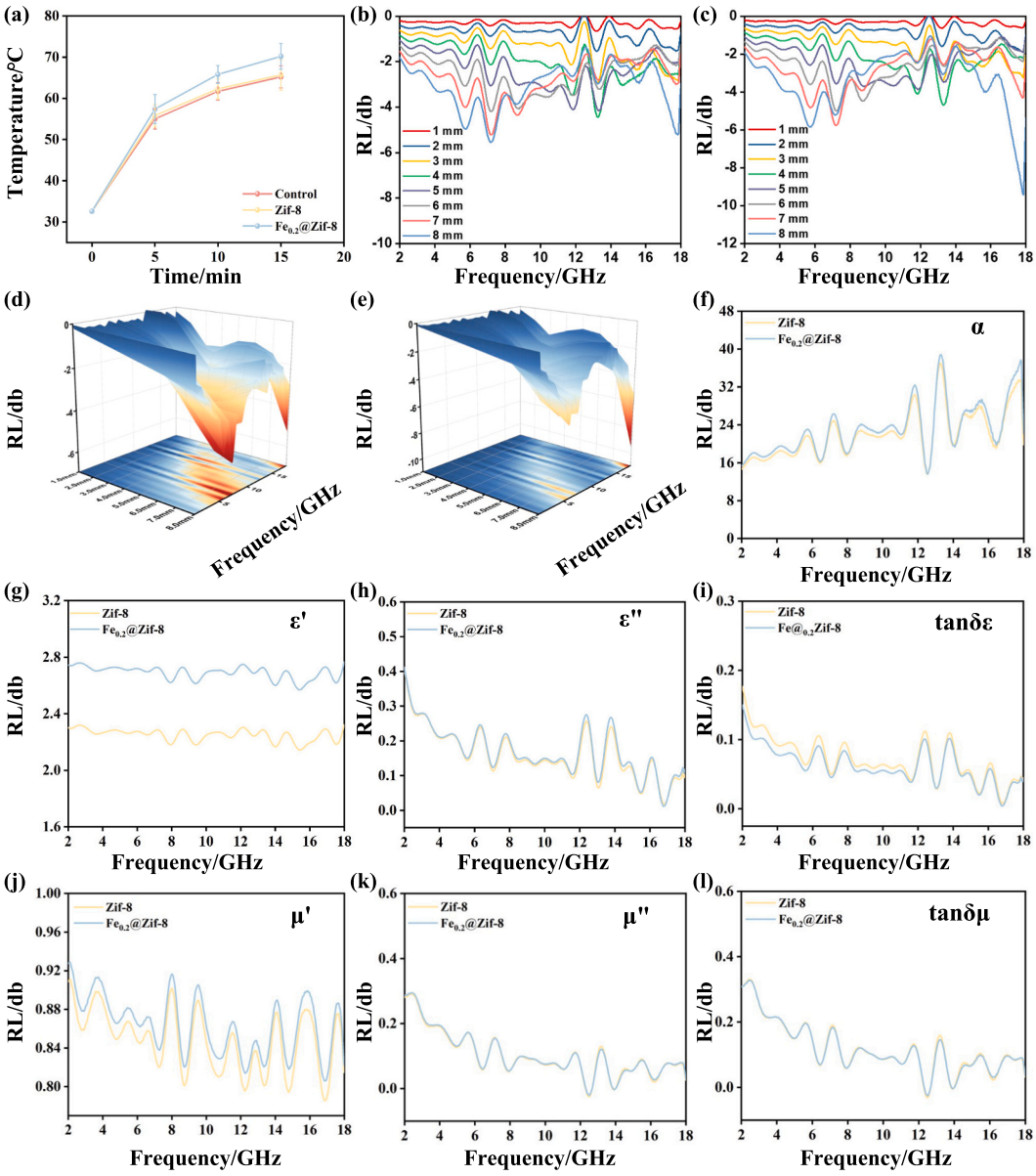

Fig. 2. (a) Heating curves of Control, Zif-8 and $Fe_{0.2}$@Zif-8 under MW irradiation; (b, c) The reflection loss (RL) curves of Zif-8 and Fe ~ 0.2 ~ @Zif-8 at varying thicknesses (A lower RL value indicates superior microwave absorption) and (d, e) frequency-dependent 3D plots for Zif-8 and $Fe_{0.2}$@Zif-8; (f) The attenuation constants of frequency for Zif-8 and $Fe_{0.2}$@Zif-8; The (k) imaginary and (l) real parts of the dielectric constants of Zif-8 and $Fe_{0.2}$@Zif-8; (i) The frequency dependence of dielectric loss tangent of Zif-8 and $Fe_{0.2}$@Zif-8; The (k) imaginary and (l) real parts of the magnetic constants of Zif-8 and $Fe_{0.2}$@Zif-8; (i) The frequency dependence of magnetic loss tangent of Zif-8 and $Fe_{0.2}$@Zif-8.

disulphide (GSSG). The GSH-consuming capacity of $Fe_{0.2}$@Zif-8 has been determined by using DTNB as a probe. As shown in Fig. 4c, after co-incubating the different groups with H_2O_2 and GSH for 15 min. The GSH consumption of $Fe_{0.2}$@Zif-8 + H_2O_2 group reaches about 30 %. However, after MW irradiation, the GSH depletion of the $Fe_{0.2}$@Zif-8 + H_2O_2 group has reached 75 %. Therefore, the GSH depletion can be accelerated by MW. Meanwhile, the GSH consumption is increased with the reaction time and the concentration of $Fe_{0.2}$@Zif-8 (Fig. 4d and e). The Fenton reaction and GSH depletion mechanism of $Fe_{0.2}$@Zif-8 are shown in Fig. 4f.

3.4. *In vitro tumor suppression efficiency*

Biosafety evaluation constitutes a fundamental prerequisite for advancing nanomaterial-based biomedical applications. To systematically assess the cytotoxic profile of $Fe_{0.2}$@Zif-8, CCK-8 assays are performed on both tumorigenic 4 T1 and normal fibroblast L929 cell lines. As shown in Fig. S5, cellular viability exhibite a concentration-dependent reduction in both cell types. In consideration of biological safety, we select the material concentration of 100 μg/mL, which ensure a normal cell survival rate exceeding 80 %, as the criterion for determining subsequent anti-tumor concentrations.

The therapeutic effects on tumor cells are verified through the CCK-8 assay and live/dead staining assay. As shown in Fig. 5a, in the absence of MW irradiation, the $Fe_{0.2}$@Zif-8 + H_2O_2 group likely induce the generation of ROS *via* a Fenton-like reaction, thereby killing a portion of tumor cells. When expose solely to MW irradiation, no significant cytotoxic effect is observed on the tumor cells. However, upon introducing $Fe_{0.2}$@Zif-8, hyperthermia-induced cytotoxicity led to the death of some tumor cells. Conversely, with the subsequent addition of H_2O_2, the synergistic effect of MWTT and CDT result in the eradication of the majority of tumor cells. Consistent with the CCK-8 results, only the

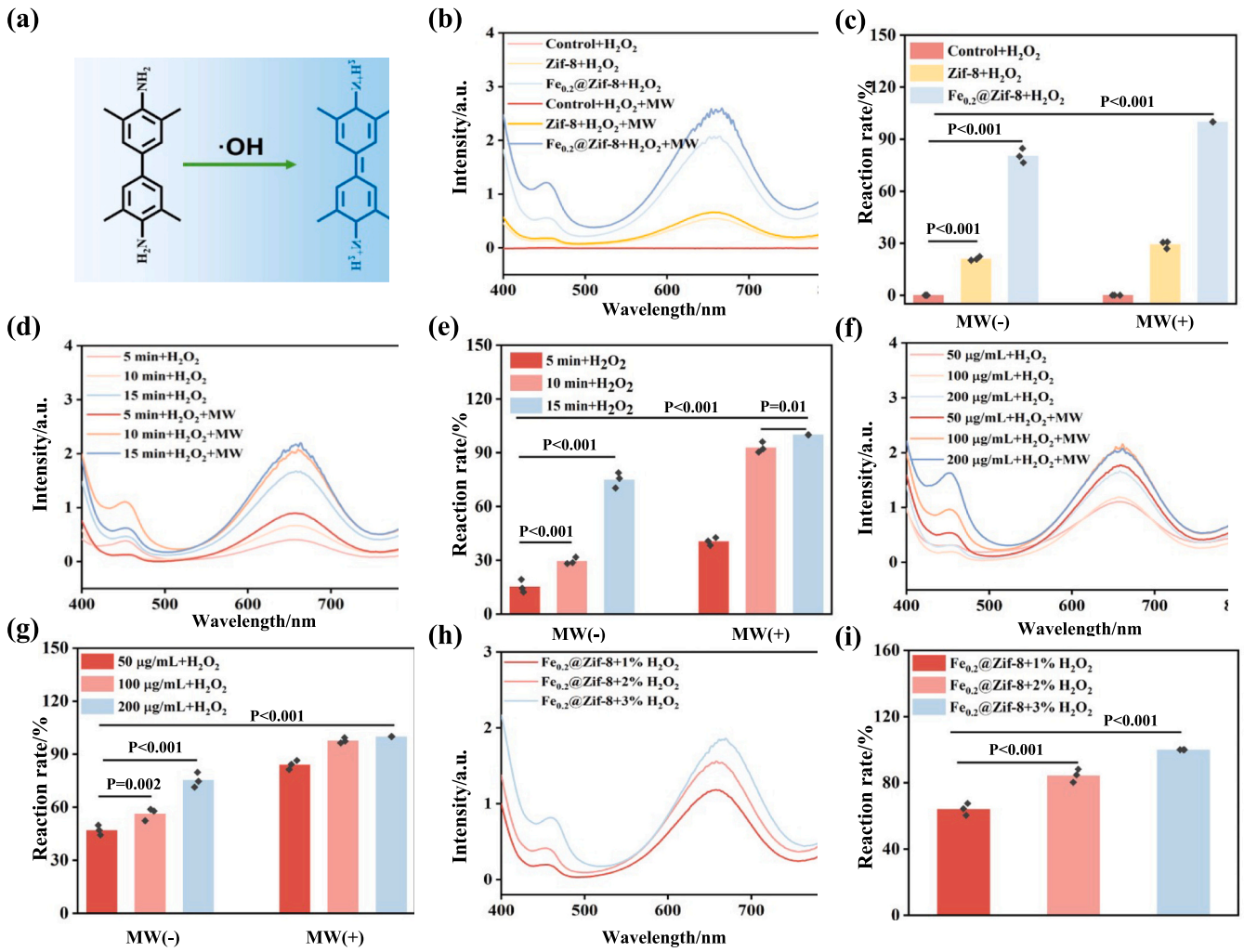

Fig. 3. (a) Schematic diagram of the oxidation of TMB to ox-TMB by ·OH; (b) UV–Vis spectra and (c) catalytic reaction rates of Zif-8 and $Fe_{0.2}$@Zif-8; (d) UV–Vis spectra and (e) catalytic reaction rates of the same concentration of $Fe_{0.2}$@Zif-8 irradiated for different times at MW; (f) UV–visible spectra and (g) catalytic reaction rates of different concentrations of $Fe_{0.2}$@Zif-8 after MW irradiation for the same time; (h) UV–Vis spectra and (i) catalytic reaction rates of the same concentration of $Fe_{0.2}$@Zif-8 under different concentrations of H_2O_2.

$Fe_{0.2}$@Zif-8 + H_2O_2 + MW group exhibit prominent red fluorescence across a large area (Fig. 5b, Fig. S6), which suggest that the synergistic effect of MWTT and CDT can efficiently induce cytotoxicity in breast cancer cells.

The efficacy of CDT is measured by evaluating intracellular ROS generation using DCFH-DA, which emits green fluorescence upon oxidation by ROS. As shown in Fig. 5c, weak green fluorescence is observed in the $Fe_{0.2}$@Zif-8 group compare with the control group. The introduction of H_2O_2 alone or MW alone can each promote ROS generation to some extent. However, when both are combined, the $Fe_{0.2}$@Zif-8 + H_2O_2 + MW group exhibit extensive green fluorescence, indicating a markedly enhance ROS production. The results of flow cytometry (Fig. 5d) are consistent with those observed under fluorescence microscopy. The fluorescence intensity is the highest in the $Fe_{0.2}$@Zif-8 + H_2O_2 + MW group, which is 8.6 times higher than that in the $Fe_{0.2}$@Zif-8 + H_2O_2 group and 6.6 times higher than that in the $Fe_{0.2}$@Zif-8 + MW group (Fig. S8).

The apoptosis of cells in the samples under MW irradiation is analyzed by flow cytometry. As shown in Fig. 5e, there is little difference among the control, $Fe_{0.2}$@Zif-8, H_2O_2, and $Fe_{0.2}$@Zif-8 + H_2O_2 groups. In contrast, a large number of cells enter the apoptosis process in the $Fe_{0.2}$@Zif-8 + MW and $Fe_{0.2}$@Zif-8 + H_2O_2 + MW groups, indicating that microwave-induced hyperthermia can promote tumor cell apoptosis. Meanwhile, more tumor cells in the $Fe_{0.2}$@Zif-8 + H_2O_2 + MW group enter late apoptosis, suggesting that the combined effect of ROS and hyperthermia can further promote the ultimate death of tumor cells.

3.5. *In vivo performance of tumor inhibition by $Fe_{0.2}$@Zif-8*

Given that $Fe_{0.2}$@Zif-8 can effectively kill breast cancer cells *in vitro*, we establish a breast cancer-bearing mouse model to evaluate its *in vivo* effect. Fig. 6a show the temperature rise curves of the samples under MW irradiation. The temperature of pure MW irradiation only rose to about 35 °C, while that of $Fe_{0.2}$@Zif-8 rose to about 48 °C. Fig. 6B show the volume changes of the tumors after 15 days of treatment. The tumor volumes of the control and Zif-8 groups significantly increase after 15 days of treatment, while the tumor volume of the $Fe_{0.2}$@Zif-8 group significantly decrease. To quantify the anti-breast cancer effect, the relative tumor volume (V/V0) is further calculated and the tumors were weighed (Fig. 6C and D). The tumor tissue changes in the control and Zif-8 groups are basically the same, with the relative tumor volume increasing to over 6 and the weight being about 1.5 g. In contrast, the relative tumor volume of the $Fe_{0.2}$@Zif-8 group decrease to 0.156 and

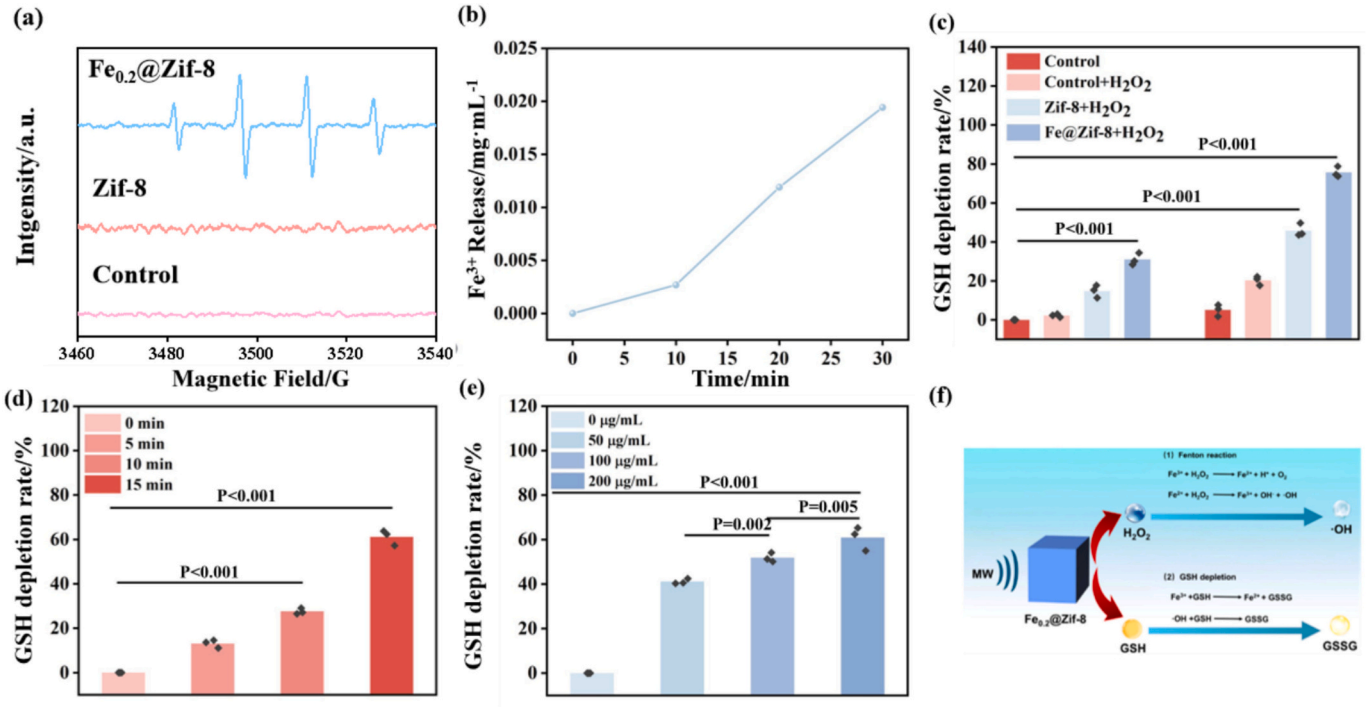

Fig. 4. (a) EPR results of the ·OH; (b) Release profiles of Fe^{3+} in PBS; (c) The depletion of GSH by different materials; Time (d) - and concentration (e) - dependent depletion of GSH from $Fe_{0.2}$@Zif-8; (f) Schematic representation of ROS production and consumption of GSH by $Fe_{0.2}$@Zif-8.

the weight is 0.267 g. H&E and TUNEL staining (Fig. 6E) show extensive cell necrosis in the breast cancer tissue of the $Fe_{0.2}$@Zif-8 group. At the same time, tumor tissue sections are stained with Ki-67 antibody to observe the proliferation activity of tumor cells in different groups. The effect of $Fe_{0.2}$@Zif-8 on the proliferation of breast cancer cells is negligible, while the Ki-67 staining images of the control and Zif-8 groups show obvious tumor cell proliferation, confirming the significant *in vivo* therapeutic effect of $Fe_{0.2}$@Zif-8 under MW irradiation.

The MRI effect of $Fe_{0.2}$@Zif-8 in tumor-bearing mice is further evaluated (Fig. 6F). Compared with 0 h, the T2 signal in the tumor tissue significantly increase 2 h after injection and then gradually decrease. This indicated that $Fe_{0.2}$@Zif-8 can effectively accumulate at the tumor site and have excellent MRI capabilities, paving the way for MRI-guided tumor treatment. To quantitatively evaluate the MRI capability of $Fe_{0.2}$@Zif-8 and allow for direct comparison with commercial contrast agents, we measured its transverse relaxation (r2). As shown in Fig. S10 A, the relaxation rate (R2) exhibited a strong linear dependence on the Fe concentration. The r2 value of $Fe_{0.2}$@Zif-8 was 23.81 mM^{-1} s^{-1} (Fig. S10 B). This high r2 value confirms Fe@Zif-8 as an effective T2 contrast agent. Furthermore, the signal-to-noise ratio (SNR) in the tumor region decreased significantly post-injection, consistent with the efficient accumulation and strong T2 contrast effect of the nanoplatform.

To comprehensively evaluate the systemic biosafety of Fe@Zif-8, the blood samples and major organs were collected for analysis (Deepika et al., 2025; Deepika et al., 2024). As shown in Table S1., the serum levels of key liver function markers (ALT, AST) and kidney function markers (BUN, CREA) in the Fe@Zif-8-treated groups showed no statistically significant differences compared to the PBS control group. Furthermore, histopathological examination (H&E staining) of the liver, kidney, and spleen (Fig. S11) revealed no obvious signs of inflammation, necrosis, or tissue damage. These results collectively demonstrate that Fe@Zif-8 does not induce significant systemic toxicity at the administered doses, confirming its favorable biosafety profile for *in vivo* applications.

The synergistic interplay between MWTT and Fenton-like reaction-driven CDT establishes $Fe_{0.2}$@Zif-8 as a dual-modal anticancer platform with optimized tumor-specific cytotoxicity. The tumor-selective potency of this multimodal strategy originates from the inherent thermosensitivity disparity between malignant and normal cells (Li et al., 2018). Previous studies have established that cancer cells exhibit compromised heat dissipation capacity due to their chaotic vasculature and hypermetabolic state, rendering them more vulnerable to hyperthermia-induced protein denaturation and organelle dysfunction (Zhang et al., 2022; Ma et al., 2020). This differential thermal tolerance aligns with reports on heat-shock protein (HSP) dysregulation in tumors, which exacerbates their susceptibility to thermal insults (Pan et al., 2021).

Microwave irradiation profoundly augments CDT efficacy through spatiotemporal coordination of physicochemical processes. The dielectric heating effect accelerates Fe^{2+}/Fe^{3+} redox kinetics - analogous to thermally enhanced Fenton catalysis observed in other iron-based nanosystems (Laha et al., 2022). Locally elevated temperatures lower the activation energy for •OH production while increasing tumor membrane fluidity to facilitate intracellular H_2O_2 diffusion, a mechanism reminiscent of photothermal-enhanced chemodynamic therapies (Chang et al., 2024).

The lethal synergy between MWTT and CDT arises from their orthogonal yet complementary attack on cellular defense mechanisms. Hyperthermia acutely disrupts protein homeostasis by denaturing chaperones like HSP70/90, thereby impairing tumor cells' ability to repair oxidative damage inflicted by ROS (Chen et al., 2023). Conversely, the oxidative stress from CDT depletes antioxidant reserves (*e.g.*, GSH), sensitizing cells to subsequent thermal insults (Yang et al., 2021b).

4. Conclusion

In summary, we have successfully engineered an iron-doped Zif-8 nanoplatform (Fe@Zif-8) that integrates MWTT and CDT for precise and efficient treatment of TNBC. The incorporation of iron ions into the Zif-8 framework not only amplifies microwave absorption through enhanced

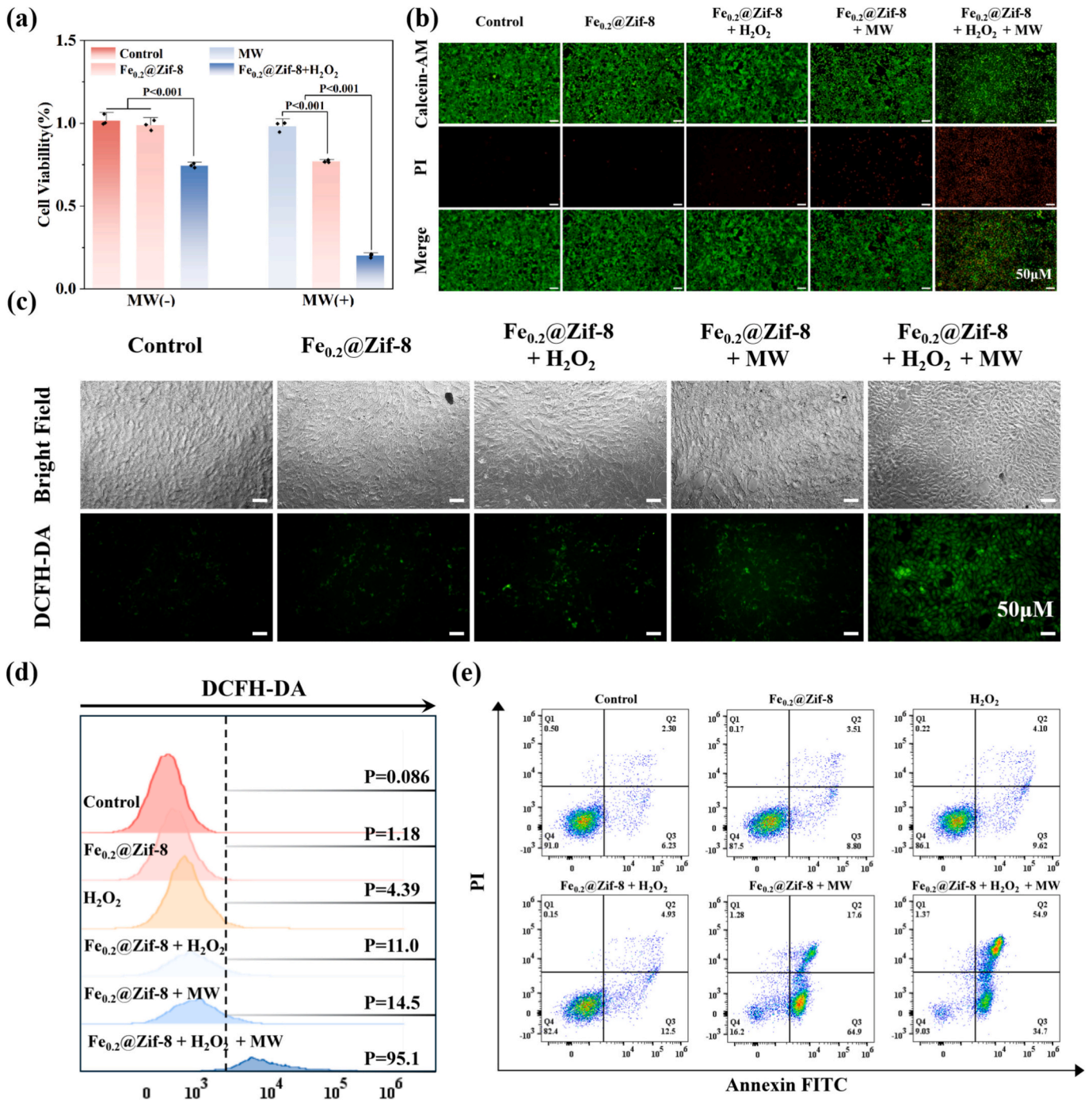

Fig. 5. (a) Effects of $Fe_{0.2}$@Zif-8 concentration on the survival rates of normal cells (L929) and cancer cells (4 T1), as detected with CCK-8 assay; (b) Fluorescence images of 4 T1 cells co-stained by Calcein-AM and PI after different treatments; (c) Fluorescence images of ROS generation in 4 T1 cells after different treatments; (d) Flow cytometry results of ROS production at cellular level; (e) Flow cytometry results of 4 T1 cell apoptosis and the percentage of early and late apoptosis of different treatments.

dielectric loss but also enables Fenton-like catalysis in the tumor TME, generating cytotoxic ROS while depleting GSH. This dual-action mechanism achieves rapid tumor ablation under low-energy MW irradiation, significantly reducing collateral damage to healthy tissues. Furthermore, the intrinsic magnetic properties of Fe@Zif-8 facilitate real-time MRI-guided tumor localization and therapeutic monitoring, underscoring its theranostic potential. This work offers a promising strategy for combating refractory malignancies like TNBC.

CRediT authorship contribution statement

Zhenyu Xiang: Formal analysis, Data curation. **Jialing Liu:** Writing – original draft, Formal analysis, Data curation. **Yan Zhang:** Investigation. **Ru Shen:** Methodology. **Ying Lu:** Project administration. **Rong Li:** Supervision, Software. **Qinying Shi:** Validation. **Guannan Zhang:** Writing – review & editing, Writing – original draft, Project administration, Formal analysis, Data curation, Conceptualization. **Sijin Li:** Visualization, Supervision. **Jianbo Song:** Funding acquisition,

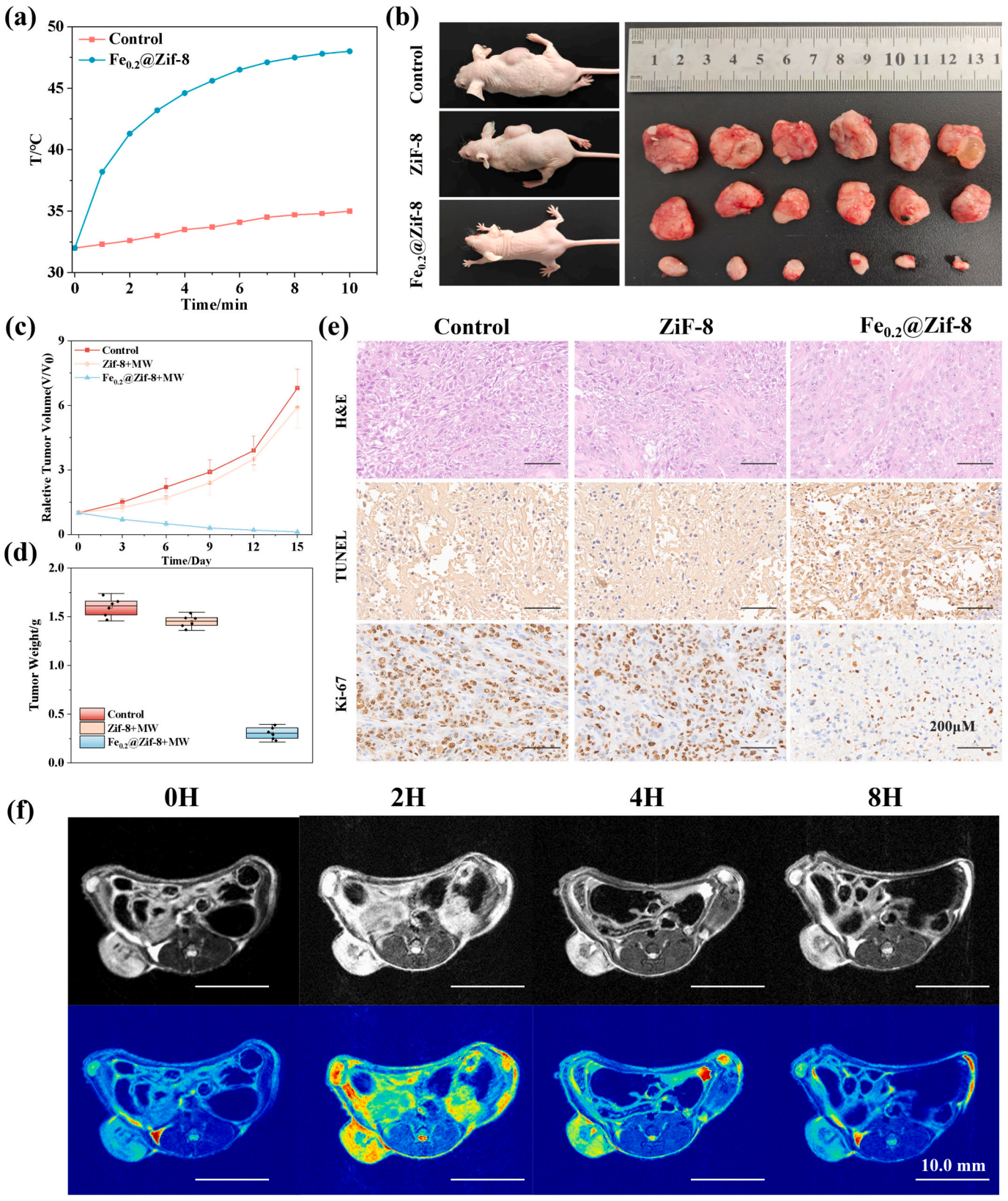

Fig. 6. (a) Infrared thermography temperature - rise curve of different treatments (5 W, 10 min); (b) Tumor volume changes during the experimental period; (c) Tumor weight in the mice after treatment; (d) Photos of male mice with tumors in each group and photographs of excised tumor tissue at 14 days after treatment; (e) Hematoxylin and eosin (H&E) staining, terminal deoxynucleotidyl transferase dUTP nick-end labeling (TUNEL) apoptosis staining,Ki-67 staining images in tumor tissues for each group; (f) T2 MRI of tumor tissues at different times after injecting $Fe_{0.2}$@Zif-8 in the tumor-bearing mouse.

Conceptualization.

Declaration of competing interest

The authors declare that they have no known competing financial interests or personal relationships that could have appeared to influence the work reported in this paper.

Acknowledgments

This work was financially supported by the National Natural Science Foundation of China (52171240), Central Leading Science and Technology Development Foundation of Shanxi Province (YDZJSX20231A064), Shanxi Province Higher Education "Billion Project" Science and Technology Guidance Project (BYYX001), Basic Projects in Research of Shanxi (Projects of Free Exploration, 202203021212095), The Foundation of Shanxi Bethune Hospital (2022RC03, 2024GSPYJ07, 2024GSPYJ21)

Appendix A. Supplementary data

Supplementary data to this article can be found online at https://doi.org/10.1016/j.ijpx.2025.100426.

Data availability

Data will be made available on request.

References

Bianchini, G., De Angelis, C., Licata, L., Gianni, L., 2022. Treatment landscape of triple-negative breast cancer—expanded options, evolving needs. Nat. Rev. Clin. Oncol. 19 (2), 91–113.

Canning, M., Liu, Y., Aldrich, J., Switchenko, J.M., Bhave, M.A., 2023. Patient understanding of immunotherapy and its side effects for women with triple negative breast cancer. J. Clin. Oncol. 41 (16_suppl) e24046-e24046.

Chang, P., Guo, Y., Chen, D., Li, K., Wang, W., Yang, Z., Ma, J., Zeng, Y., Zhan, W., Zhan, Y., 2024. High-temperature PTT/CDT coordination nanoplatform realizing exacerbated hypoxia for enhancing hypoxia-activated chemotherapy to overcome tumor drug resistance. J. Nanobiotechnol. 22 (1), 374.

Chen, Z., Li, S., Li, F., Qin, C., Li, X., Qing, G., Wang, J., Xia, B., Zhang, F., Meng, L., 2023. DNA damage inducer mitoxantrone amplifies synergistic mild-photothermal chemotherapy for TNBC via decreasing heat shock protein 70 expression. Adv. Sci. 10 (16), 2206707.

Cheung, E.C., Vousden, K.H., 2022. The role of ROS in tumour development and progression. Nat. Rev. Cancer 22 (5), 280–297.

Cui, H., Zhao, Y.Y., Wu, Q., You, Y., Lan, Z., Zou, K.L., Cheng, G.W., Chen, H., Han, Y.H., Chen, Y., 2024. Microwave-responsive gadolinium metal-organic frameworks nanosystem for MRI-guided cancer thermotherapy and synergistic immunotherapy. Bioactive Mater. 33, 532–544.

Dai, J., Xiao, X., Duan, S., Liu, J., He, J., Lei, J., et al., 2018. Synthesis of novel microporous nanocomposites of ZIF-8 on multiwalled carbon nanotubes for adsorptive removing benzoic acid from water. Chem. Eng. J. 331, 64–74.

Deepika, B., Gowtham, P., Raghavan, V., Isaac, J.B., Devi, S., Kiran, V., Mercy, D.J., Sofini, P.S.S., Harini, A., Girigoswami, A., Girigoswami, K., 2024 Oct. Harmony in nature's elixir: a comprehensive exploration of ethanol and nano-formulated extracts from Passiflora incarnata leaves: unveiling in vitro cytotoxicity, acute and sub-acute toxicity profiles in Swiss albino mice. J. Mol. Histol. 55 (5), 977–994.

Deepika, B., Janani, G., Jessy Mercy, D., Udayakumar, S., Girigoswami, A., Girigoswami, K., 2025 Feb 18. Inhibitory effect of Nano-Formulated Extract of *Passiflora incarnata* on Dalton's Lymphoma Ascites-Bearing *Swiss albino* mice. Pharmaceutics 17 (2), 270.

Fu, A.Z., Kuang, Y., Fazeli, M.S., Kumar, N., Davis, C., 2019. Current treatment landscape in triple negative breast cancer: a systematic literature review. Ann. Oncol. 30 iii55–6.

Gong, W., Chen, Z., Dong, J., Liu, Y., Cui, Y., 2022. Chiral metal-organic frameworks. Chem. Rev. 122 (9), 9078–9144.

Gowtham, P., Girigoswami, K., Pallavi, P., Harini, K., Gurubharath, I., Girigoswami, A., 2022 Nov 22. Alginate-Derivative Encapsulated Carbon Coated Manganese-Ferrite Nanodots for Multimodal Medical Imaging. Pharmaceutics 14 (12), 2550.

Haggag, R.M., Abu-Taleb, F.M., Elsayed, H., Shiha, A., 2022. 16P the prognostic value of androgen receptor expression in triple-negative breast cancer patients. Ann. Oncol. 33, S1436.

Jin, L., Zheng, Y., Liu, X., Zhang, Y., Li, Z., Liang, Y., Zhu, S., Jiang, H., Cui, Z., Wu, S., 2022. Magnetic composite rapidly treats Staphylococcus aureus-infected osteomyelitis through microwave strengthened thermal effects and reactive oxygen species. Small 18 (41), 2204028.

Jin, X., Shan, J., Zhao, J., Wang, T., Zhang, W., Yang, S., Qian, H., Cheng, L., Chen, X.L., Wang, X., 2024. Bimetallic oxide Cu-Fe_3O_4 nanoclusters with multiple enzymatic activities for wound infection treatment and wound healing. Acta Biomater. 173, 403–419.

Kong, C., Xu, B., Qiu, G., Wei, M., Zhang, M., Bao, S., Tang, J., Li, L., Liu, J.J., 2022. Multifunctional nanoparticles-mediated ptt/pdt synergistic immune activation and antitumor activity combined with anti-PD-L1 immunotherapy for breast cancer treatment. Int. J. Nanomedicine 17, 5391.

Laha, S.S., Thorat, N.D., Singh, G., Sathish, C.I., Yi, J., Dixit, A., Vinu, A., 2022. Rare-earth doped iron oxide nanostructures for cancer theranostics: magnetic hyperthermia and magnetic resonance imaging. Small 18 (11), 2104855.

Lancet, T., 2017. Breast cancer targeted therapy: successes and challenges. Lancet (London, England) 389 (10087), 2350.

Li, N., Zhou, L., Jin, X., Owens, G., Chen, Z., 2019. Simultaneous removal of tetracycline and oxytetracycline antibiotics from wastewater using a ZIF-8 metal organic-framework. J. Hazard. Mater. 366, 563–572.

Li, S., Tan, L., Meng, X., 2020. Nanoscale metal-organic frameworks: synthesis, biocompatibility, imaging applications, and thermal and dynamic therapy of tumors. Adv. Funct. Mater. 30 (13), 1908924.

Li, S., Chen, Z., Tan, L., Wu, Q., Ren, X., Fu, C., Niu, M., Li, H., Meng, X., 2022. MOF@COF nanocapsule for the enhanced microwave thermal-dynamic therapy and anti-angiogenesis of colorectal cancer. Biomaterials 283, 121472.

Li, S., Xu, F., Ren, X., Tan, L., Fu, C., Wu, Q., Chen, Z., Ren, J., Huang, Z., Meng, X., 2023. H_2S-reactivating antitumor immune response after microwave thermal therapy for long-term tumor suppression. ACS Nano 17 (19), 19242–19253.

Li, S., Chen, Z., Guo, W., Tan, L., Wu, Q., Ren, X., Fu, C., Wang, Q., Huang, Z., Meng, X., 2024. H_2S-mediated gas therapy and HSP90 downregulation synergically enhance tumor microwave thermal therapy. Adv. Funct. Mater. 34 (21), 2314742.

Li, W., Samarasinghe, S.A., Bae, T.H., 2018. Enhancing CO_2/CH_4 separation performance and mechanical strength of mixed-matrix membrane via combined use of graphene oxide and ZIF-8. J. Ind. Eng. Chem. 67, 156–163.

Lin, X., Liu, S., Zhang, X., Zhu, R., Chen, S., Chen, X., Song, J., Yang, H., 2020. An ultrasound activated vesicle of janus Au-MnO nanoparticles for promoted tumor penetration and sono-chemodynamic therapy of orthotopic liver cancer. Angew. Chem. 132 (4), 1699–1705.

Lv, Y., Chen, C., Jin, L., Zheng, Y., Wu, S., Zhang, Y., Li, Z., Zhu, S., Jiang, H., Cui, Z., 2023. Microwave-excited, antibacterial core-shell $BaSO_4/BaTi_5O_{11}$@PPy heterostructures for rapid treatment of S. aureus-infected osteomyelitis. Acta Biomater. 167, 506–518.

Ma, L., Feng, X., Liang, H., Wang, K., Song, Y., Tan, L., Wang, B., Luo, R., Liao, Z., Li, G., 2020. A novel photothermally controlled multifunctional scaffold for clinical treatment of osteosarcoma and tissue regeneration. Mater. Today 36, 48–62.

Pallavi, P., Girigoswami, K., Gowtham, P., Harini, K., Thirumalai, A., Girigoswami, A., 2024. Encapsulating Rhodamine 6G in Oxidized Sodium Alginate Polymeric Hydrogel for Photodynamically Inactivating Cancer Cells. Curr. Pharm. Des. 30 (35), 2801–2812.

Pan, J., Xu, Y., Wu, Q., Hu, P., Shi, J., 2021. Mild magnetic hyperthermia-activated innate immunity for liver cancer therapy. J. Am. Chem. Soc. 143 (21), 8116–8128.

Pan, X., Bai, L., Wang, H., Wu, Q., Wang, H., Liu, S., Xu, B., Shi, X., Liu, H., 2018. Metal-organic-framework-derived carbon nanostructure augmented sonodynamic cancer therapy. Adv. Mater. 30 (23), 1800180.

Schade, A.E., Perurena, N., Yang, Y., Rodriguez, C.L., Krishnan, A., Gardner, A., Loi, P., Xu, Y., Nguyen, V.T., Mastellone, G.J.N., 2024. AKT and EZH2 inhibitors kill TNBCs by hijacking mechanisms of involution. Nature 635 (8039), 755–763.

Siegel, R.L., Miller, K.D., Fuchs, H.E., Jemal, A., 2022. Cancer statistics, 2022. CA Cancer J. Clin. 72 (1), 7–33.

Thirumalai, A., Girigoswami, K., Pallavi, P., Harini, K., Gowtham, P., Girigoswami, A., 2023 Dec. Cancer therapy with iRGD as a tumor-penetrating peptide. Bull. Cancer 110 (12), 1288–1300.

Thirumalai, A., Girigoswami, K., Prabhu, A.D., Durgadevi, P., Kiran, V., Girigoswami, A., 2024 Oct 26. 8-Anilino-1-naphthalenesulfonate-Conjugated Carbon-Coated Ferrite Nanodots for Fluoromagnetic Imaging, Smart Drug delivery, and Biomolecular Sensing. Pharmaceutics 16 (11), 1378.

Truong Hoang, Q., Huynh, K.A., Nguyen Cao, T.G., Kang, J.H., Dang, X.N., Ravichandran, V., Kang, H.C., Lee, M., Kim, J.E., Ko, Y., 2023. Piezocatalytic 2D WS_2 nanosheets for ultrasound-triggered and mitochondria-targeted piezodynamic cancer therapy synergized with energy metabolism-targeted chemotherapy. Adv. Mater. 35 (18), 2300437.

Wang, J., Ding, H., Zhu, Y., Liu, Y., Yu, M., Cai, H., Ao, R., Huang, H., Gong, P., Liao, Y., 2023. Iron-siRNA nanohybrids for enhanced chemodynamic therapy via ferritin heavy chain downregulation. Angew. Chem. 135 (22), e202302255.

Wang, X., Zhong, X., Liu, Z., Cheng, L., 2020. Recent progress of chemodynamic therapy-induced combination cancer therapy. Nano Today 35, 100946.

Wu, S., Liu, H., Yang, C., Li, X., Lin, Y., Yin, K., Sun, J., Teng, Q., Du, C., Zhong, Y., 2020. High-performance porous carbon catalysts doped by iron and nitrogen for degradation of bisphenol F via peroxymonosulfate activation. Chem. Eng. J. 392, 123683.

Yang, H., Hu, S., Zhao, H., Luo, X., Liu, Y., Deng, C., Wang, L., 2021a. High-performance Fe-doped ZIF-8 adsorbent for capturing tetracycline from aqueous solution. J. Hazard. Mater. 416, 126046.

Yang, L., Hou, X., Zhang, Y., Wang, D., Liu, J., Huang, F., Liu, J., 2021b. NIR-activated self-sensitized polymeric micelles for enhanced cancer chemo-photothermal therapy. J. Control. Release 339, 114–129.

Yang, X., Zhang, H., Wu, Z., Chen, Q., Zheng, W., Shen, Q., Wei, Q., Shen, J.W., Guo, Y., 2024. Tumor therapy utilizing dual-responsive nanoparticles: a multifaceted

approach integrating calcium-overload and PTT/CDT/chemotherapy. J. Control. Release 376, 646–658.
Yuan, J., Wang, J., Song, M., Zhao, Y., Shi, Y., Zhao, L., 2024. Brain-targeting biomimetic disguised manganese dioxide nanoparticles via hybridization of tumor cell membrane and bacteria vesicles for synergistic chemotherapy/chemodynamic therapy of glioma. J. Colloid Interface Sci. 676, 378–395.
Zhang, G., Wu, Z., Yang, Y., Shi, J., Lv, J., Fang, Y., Shen, Z., Lv, Z., Li, P., Yao, X., Chen, W., Wei, X., Chu, P.K., Zhang, X., 2022. A multifunctional antibacterial coating on bone implants for osteosarcoma therapy and enhanced osteointegration. Chem. Eng. J. 428, 131155.
Zhao, B., Ma, Z., Ding, S., Cao, Y., Du, J., Zeng, L., Hu, Y., Zhou, J., Zhang, X., Bian, X., 2023. Catalytic $MnWO_4$ nanorods for chemodynamic therapy synergized radiotherapy of triple negative breast cancer. Adv. Funct. Mater. 33 (47), 2306328.
Zhu, Y., Li, Q., Wang, C., Hao, Y., Yang, N., Chen, M., Ji, J., Feng, L., Liu, Z., 2023. Rational design of biomaterials to potentiate cancer thermal therapy. Chem. Rev. 123 (11), 7326–7378.